Chinese Chemical Letters 35 (2024) 110025

Contents lists available at ScienceDirect

Chinese Chemical Letters

journal homepage: www.elsevier.com/locate/cclet

20 nm-ultra-thin fluorosiloxane interphase layer enables dendrite-free, fast-charging, and flexible aqueous zinc metal batteries

Yuhuan Meng[a], Long Zhang[b,*], Lequan Wang[a], Junming Kang[a], Hongbin Lu[a,c,*]

[a] State Key Laboratory of Molecular Engineering of Polymers, Department of Macromolecular Science, Fudan University, Shanghai 200438, China
[b] School of Materials Science and Engineering, University of Science and Technology Beijing, Beijing 100083, China
[c] Yiwu Research Institute of Fudan University, Yiwu 322000, China

ARTICLE INFO

Article history:
Received 26 January 2024
Revised 16 May 2024
Accepted 17 May 2024
Available online 17 May 2024

Keywords:
Siloxane
High current density
Zinc dendrite
Fast-charging
Flexible device

ABSTRACT

Dendrite growth of zinc (Zn) anode at high current density severely affects the fast-charging performance of aqueous zinc metal batteries (AZMBs). While interfacial modification strategies can optimize Zn performance, challenges such as complicated preparation processes, excessive layer thicknesses, and high voltage hysteresis should be addressed. Herein, we utilize a cost-effective liquid fluorosiloxane, (3,3,3-trifluoropropyl)trimethoxysilane, for scalable modification of Zn foil *via* drop-casting at room temperature, resulting in an ultra-thin interphase layer of only 20 nm. The Si-O-Zn bonds formed between fluorosiloxane and Zn ensure interfacial stability, and the Si-O-Si bonds between fluorosiloxane molecules help to homogenize the electric field distribution. Additionally, the abundant highly electronegative fluorine atoms on the anode surface act as zincophilic sites, promoting the uniform deposition of Zn^{2+}. Thus, the modified Zn foil (SiFO-Zn) exhibits excellent dendrite suppression, reduced voltage hysteresis, and prolonged cycle life at ultra-high current density (40 mA/cm^2), achieving a cumulative areal capacity of 12.9 Ah/cm^2. Further, the full cell assembled with 10 μm-thick SiFO-Zn anode and MnO_2 cathode achieves 2600 cycles at 5 A/g with minimal capacity degradation, and a large-size (22.5 cm^{-2}) pouch cell powers the light-emitting diode even after reverse bending, demonstrating the potential of AZMBs for fast-charging flexible devices.

The large-scale application of clean and renewable energy has derived an urgent need for high-performance and low-cost energy storage systems [1–3]. Under this background, aqueous zinc metal batteries (AZMBs) have re-entered the field of vision by virtue of the high abundance and volumetric capacity (5855 mAh/cm^3) of zinc (Zn) anode, as well as the high safety and ionic conductivity of aqueous electrolytes, showing promising application prospects in the field of fast-charging and flexible devices [4–7]. However, the phenomenon of "savage growth" of Zn dendrites under high current density has been widely reported [8–13]. Achieving a breakthrough in Zn anode performance is a prerequisite for AZMBs to play a role in high-power electronic devices.

It has been reported that the Zn deposition morphology at high current density is dominated by the mass transfer process [14]. Specifically, more Zn^{2+} struggles to be transported to the fast Zn^{2+}-consuming anode surface, creating concentration polarization that drives inhomogeneous deposition at the interface, ultimately leading to rampant Zn dendrites. Numerous strategies have been developed for the optimization of Zn anode, among which the incorporation of electrolyte additives (glucose [15], silicon nanoparticles [16]) and three-dimensional structural design of the anode (Cu foam [17], Zn micromesh [18]) are effective in improving the deposition morphology. However, the current parameters tested in these reports are typically ≤5 mA/cm^2, and these optimization strategies may fail at higher current densities.

The interfacial modification strategy demonstrates a more pronounced effect at high current density [19,20]. The reported interphase layers for Zn anode usually contain highly electronegative elements such as fluorine (F), phosphorus (P) and nitrogen (N) [21–24], which act as zincophilic sites to induce homogeneous nucleation of Zn^{2+}, and form a flat and dense deposition morphology at current densities up to 10 mA/cm^2 (such as FCOF [25], fluorinated graphite [26], $Ca_5(PO_4)_3F$ [27], and $C_3H_{12}NO_9P_3$ [28]). Yet, the accompanied issues such as complicated preparation processes, excessive layer thicknesses (μm level), and high voltage hysteresis are inevitable. More recently, it has been reported that highly (002)-oriented Zn anodes can be obtained on various substrates by applying extremely high current density (≥80 mA/cm^2) in the

* Corresponding authors.
E-mail addresses: zhanglong@ustb.edu.cn (L. Zhang), hongbinlu@fudan.edu.cn (H. Lu).

https://doi.org/10.1016/j.cclet.2024.110025
1001-8417/

electroplating bath where the mass transfer limitation process is considerably weakened, and such Zn anodes can be cycled at current densities up to 20 mA/cm^2 [29,30]. Nevertheless, the large consumption of electrolyte and the energy consumption from the electroplating process may increase the manufacturing cost of AZMBs. Overall, it is urgent to find a more economical and feasible interfacial modification strategy for Zn anodes.

Siloxane is a class of organic molecules commonly used in metal surface treatment, which can form interphase layer on hydroxyl–rich metal surface through self-assembly (*i.e.*, hydrolysis) [31–33]. Siloxane molecules are cost-effective, environmentally friendly, non-toxic, diverse, and highly structurally designable. Up to now, the most commonly used NH_2-containing siloxane in industry, (3-aminopropyl)triethoxysilane, has been applied to modify Zn anode. For instance, Kim *et al*. obtained a hydrophilic polysiloxane layer with a thickness of 500 nm by first soaking the Zn foil in an ethanol/water/siloxane solution with a volume ratio of 95:5:5 at pH 4, followed by drying and thermal curing [34], while Qian *et al*. obtained a hydrophobic layer with a thickness of 3.5 μm by varying the hydrolysis pH to 11 [35]. The Zn foils acquired above were able to cycle for 600 h (5 mAh/cm^2) and 300 h (10 mAh/cm^2) at a current density of 20 mA/cm^2, respectively, demonstrating competitive performance. In addition, Zhong *et al*. constructed a waterglass interphase layer with a thickness of 4 μm, revealing the important role of Si-O functional groups in homogenizing the electric field distribution and inhibiting the growth of dendrites [36]. Still, the defects of common interfacial modification strategies, such as preparation issues and layer thickness, are not completely avoided. Whether AZMBs can exhibit excellent performance at even higher current densities deserves further investigation as well.

Herein, an inexpensive liquid fluorosiloxane, (3,3,3-trifluoropropyl)trimethoxysilane, is chosen for the modification of Zn foil. Unlike the conventional dip-coating followed by thermal curing, a direct drop-casting preparation method is adopted. Specifically, the fluorosiloxane is dropwise added to the O_2 plasma-treated Zn foil, which is then placed in an environment with 25 °C and 65%RH for 48 h. After being deliquesced by the moisture in air, the siloxane eventually forms an ultra-thin interphase layer of only 20 nm on the Zn surface, thus avoiding the excessive introduction of inactive substances. In the interphase layer, the formation of Si-O-Zn bonds can ensure the interfacial stability, the uniformly formed Si-O-Si network can facilitate the uniform electric field distribution, and the F atoms, with higher electronegativity than N atoms, can act as zincophilic sites to guide the homogeneous Zn^{2+} deposition. Accordingly, the modified Zn foil (SiFO-Zn) achieves 1290 cycles at ultra-high current density of 40 mA/cm^2, with a cumulative areal capacity of 12.9 Ah/cm^2. When 10 μm-thick SiFO-Zn anode is matched with MnO_2 cathode, the full cell exhibits an excellent lifespan of 2600 cycles at 5 A/g (corresponding to a high current density of 17.5 mA/cm^2 for the anode) with minimal capacity degradation observed. Further matched with a higher mass-loading MnO_2 cathode (6.25 mg/cm^2), the assembled flexible large-size (22.5 cm^{-2}) pouch cell not only lights up the light-emitting diode (LED) after reverse bending, but also exhibits excellent cycling performance at 1 A/g. In conclusion, the industrially available and inexpensive fluorosiloxane can easily achieve scalable modification of Zn foil, which exhibits superior dendrite suppression at high current densities, paving the way for the development of fast-charging flexible AZMBs.

The preparation process of SiFO-Zn anode is shown in Fig. 1a. The field emission scanning electron microscopy (FESEM) image of SiFO-Zn and the corresponding energy dispersive spectrometer (EDS) images of Zn, F, Si, O, and C confirm the homogeneous distribution of (3,3,3-trifluoropropyl)trimethoxysilane molecules on the Zn foil surface, as shown in Figs. 1b–e and Fig. S1 (Supporting information). Encouragingly, (3,3,3-trifluoropropyl)trimethoxysilane is inexpensive with a cost of only 5.5 RMB/kg, permitting rapid and scalable modification of Zn, with the distinct advantages of low energy consumption for the preparation process and homogeneous distribution for the interphase layer. Unlike reported interphase layers of Zn foil with excessive thicknesses of 2-10 μm, which lead to a significant loss of battery energy density, the room-temperature reaction conditions and trace moisture environments in this work allow the fluorosiloxane to undergo a lower degree of hydrolysis and condensation reactions, resulting in a reduced coating thickness. The fluorosiloxane interphase layer can be observed in the cross-sectional SEM image, as shown in Fig. 1f. The atomic force microscopy (AFM) image reveals its exact thickness of only 20 nm (Fig. 1g).

In order to reveal the formation mechanism of the interphase layer, the contact angle tester was first employed to characterize the changes in Zn hydrophilicity. As shown in Fig. 1h, the bare Zn foil is relative hydrophobic with a contact angle of 94.2°. The subsequent O_2 plasma treatment leads to the enrichment of hydroxyl groups on the Zn surface, as evidenced by the increase in the intensity of the O–H stretching vibration at 3470 cm^{-1} (Fig. 1i) [37]. Therefore, the hydrophilicity of Zn foil is enhanced [38] and the contact angle is reduced to 49.4°, promoting the condensation reaction between fluorosiloxane and Zn. As for SiFO-Zn, stretching vibration peaks of CH_3, CH_2, Si-O-C and CF_3 appear at 2950, 2926, 1081 and 1038 cm^{-1}, respectively, preliminarily indicating the presence of fluorosiloxane molecules on the Zn foil surface [39]. Meanwhile, the contact angle of SiFO-Zn is 85.4°, demonstrating that the trifluoromethyl groups in the molecules are conducive to increasing the hydrophobicity of the electrode. The above Fourier transform infrared (FTIR) result of SiFO-Zn is corroborated by the Raman spectrum (Fig. S2 in Supporting information). Specifically, the Si-O-H and H_2O Raman peaks confirm the hydrolysis reaction of fluorosiloxane on the electrode [40,41], with the observation of Si-O-C and CF_3 vibrations hindered by the weak Raman signal. Subsequently, X-ray photoelectron spectrometer (XPS) was employed to further investigate the interfacial properties of SiFO-Zn (Figs. 1j-m and Fig. S3 in Supporting information). The overall XPS spectrum and the CF_3 bond peaks in the C 1s and F 1s spectra (with binding energies of 293 eV and 688.6 eV, respectively) indicate the existence of fluorosiloxane, consistent with the aforementioned conclusions [42]. Notably, the peaks with binding energies of 531.8 eV and 102 eV in the O 1s and Si 2p spectra are attributed to Si-O-Zn bonds [35], confirming the covalent bonding interactions between fluorosiloxane and hydroxylated Zn surface, which is beneficial for improving the interfacial stability. Meanwhile, the Si-O peaks with binding energies of 103.2 eV (Si 2p) and 532.9 eV (O 1s) can be assigned to Si-O-Si, Si-O-C, and Si-O-H bonds due to the incomplete hydrolysis and intermolecular condensation reactions of the molecules [37,43,44], contributing to the even electric field distribution as demonstrated in the previous reports [36]. In summary, the formation process of the fluorosiloxane interphase layer on Zn surface is illustrated in Fig. 2a.

As mentioned above, the fluorosiloxane interphase layer features abundant F atoms and uniformly distributed Si-O-Si and Si-O-Zn bonds, which may benefit for SiFO-Zn to inhibit dendrites at high current density. Under this premise, the chronoamperometric (CA) tests were conducted on symmetric cells. The nucleation and growth processes of Zn^{2+} on bare Zn, treated Zn, and SiFO-Zn anodes were reflected by the corresponding *I-t* curves. As depicted in Fig. 3a, the bare Zn undergoes a prolonged two-dimensional (2D) diffusion process with an increase in current density for nearly 175 s, during which Zn^{2+} continuously diffuses to the high-potential sites on the electrode surface, inducing rampant Zn dendrites [2,13,45]. In contrast, the uniform distribution of Si-O-Si eliminates the high-potential sites on the SiFO-Zn surface, the F atoms induce direct nucleation at the Zn^{2+} adsorption site,

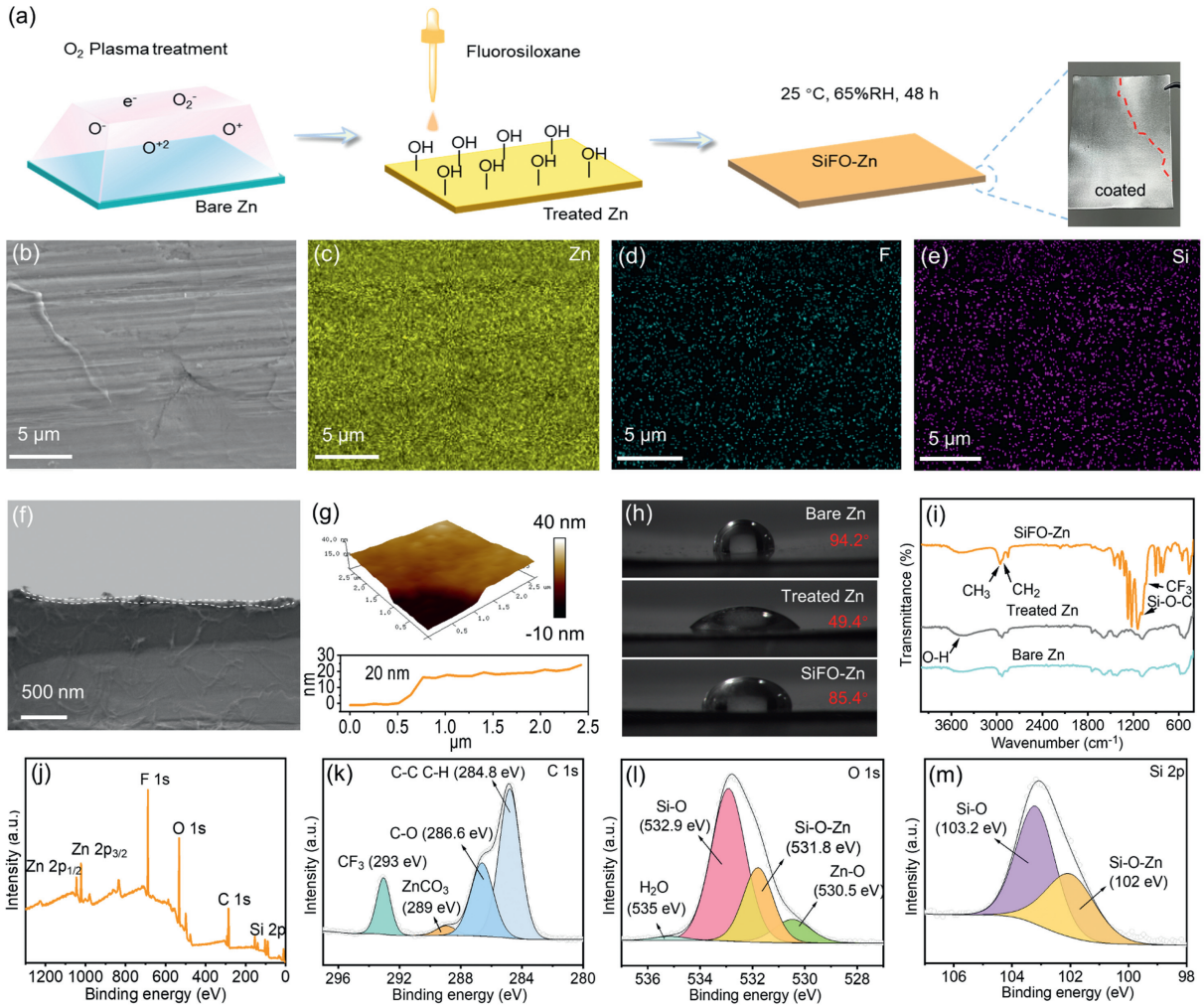

Fig. 1. (a) The preparation process of SiFO-Zn anode. (b) Surface SEM image of SiFO-Zn and the corresponding (c) Zn, (d) F and (e) Si EDS images. (f) Cross-sectional SEM image of SiFO-Zn. (g) AFM 3D height image of the fluorosiloxane interphase layer with a scanning area of 2.5 μm × 2.5 μm. (h) Contact angle (using 2 mol/L $ZnSO_4$ electrolyte) and (i) FTIR tests for bare Zn, treated Zn and SiFO-Zn. (j) Overall XPS spectrum of SiFO-Zn and the corresponding (k) C 1s, (l) O 1s and (m) Si 2p spectra.

and the Si-O-Zn bonds guarantee the interfacial stability. Under this circumstance, the symmetric cell assembled with SiFO-Zn exhibits a shortened 2D diffusion process (115 s), and a prolonged cycle life at 5 mAh/cm^2 and 10 mA/cm^2 (910 h for SiFO-Zn *vs.* 90 h for Zn, Fig. 3b). The treated Zn exhibits the shortest 2D diffusion process of only 44 s, due to the introduced hydroxyl groups that favor the wetting of the electrolyte and the uniform dispersion of Zn^{2+} at the interface [46]. However, the resulting excessive hydrophilicity of the anode leads to severe side reactions, such as corrosion and hydrogen evolution [19]. Therefore, the symmetric cell suffers from drastic polarization fluctuations during cycling, which indicates an unstable Zn deposition and dissolution process, ultimately resulting in an unsatisfactory cycle life (65 h).

Furthermore, the electrochemical impedance spectroscopy (EIS) curves of symmetric cells assembled with bare Zn, treated Zn, and SiFO-Zn were tested before and after 10 cycles at 0.5 mAh/cm^2 and 10 mA/cm^2. As shown in Fig. S4 (Supporting information), the symmetric cell assembled with treated Zn demonstrates the lowest initial charge transfer resistance (R_{ct}) of 52.1 Ω. After cycling, the R_{ct} increases dramatically to 183.7 Ω and the curves show two electrochemical interphases, as a result of by-product generation caused by excessive hydrophilicity of treated Zn [13,47]. In the case of SiFO-Zn||SiFO-Zn and Zn||Zn symmetric cells, the R_{ct} of SiFO-Zn||SiFO-Zn is lower both before and after cycling (before cycling: 55 Ω *vs.* 76.9 Ω; after cycling: 164.4 Ω *vs.* 199 Ω), indicating its superior charge transfer kinetics [48]. The specific fitting data of R_{ct} is given in Table S1 (Supporting information). In addition, the contact angles of bare Zn, treated Zn, and SiFO-Zn after cycling are shown in Fig. S5 (Supporting information).

To investigate the chemical composition changes of SiFO-Zn after cycling, the XPS, FTIR and Raman spectra were tested. As shown in Fig. S6 (Supporting information), due to the repeated deposition/stripping of Zn, the intensity of Zn $2p_{1/2}$ and $2p_{3/2}$ peaks increases significantly, with a decrease in binding energy [16,35]. Moreover, the CF_3 bond peaks almost disappear in the overall XPS and F 1s spectra, with no presence in C 1s spectrum. As the mentioned role of F atoms in inducing Zn^{2+} deposition, the disappearance of the peaks could be a result of the deposited Zn covering F-atom sites and reducing the signal intensity of CF_3. Besides, owing to the complete hydrolysis of Si-O-C, the C–O peak disappears in the C 1s spectrum, and the binding energies of Si-O peaks in the O 1s and Si 2p spectra decrease, whereas the Si-O-Zn bond peaks still exist, indicating high interfacial stability between fluorosiloxane and Zn [49]. The results of FTIR and Raman tests (Fig. S7 in Supporting information) are in agreement with the above XPS findings, verifying the conclusions of the CA test.

To further assess the dendrite inhibition effect of the fluorosiloxane interphase layer, the surface morphologies of bare

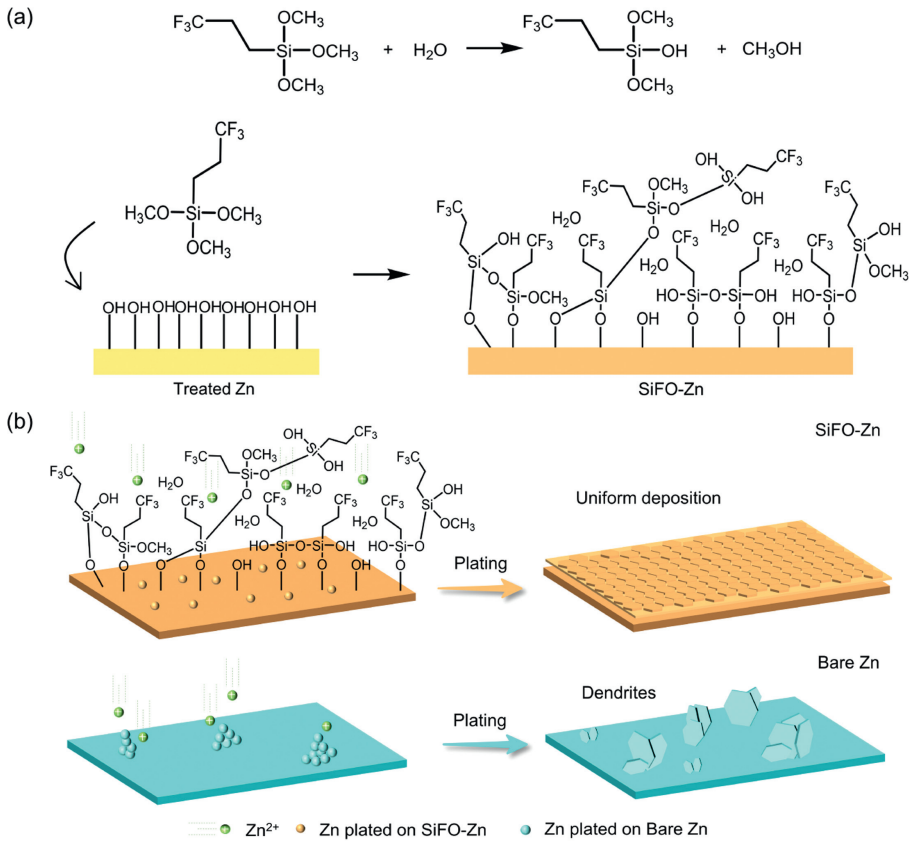

Fig. 2. Schematic diagrams of (a) the formation process of fluorosiloxane interphase layer on Zn and (b) the Zn^{2+} deposition process on SiFO-Zn and bare Zn.

Zn and SiFO-Zn anodes were observed after Zn deposition at 10 mA/cm^2 for 30 min. AFM 3D height image (Fig. 3c) shows the appearance of distinct "tips" on the bare Zn surface after deposition of 5 mAh/cm^2, which may deteriorate and eventually pierce the separator. The SEM image of bare Zn (Fig. 3d) also demonstrates numerous sword-like Zn dendrites. On the contrary, the AFM image of SiFO-Zn (Fig. 3e) exhibits a dense and flat morphology, and the SEM image (Fig. 3f) shows small-sized Zn flakes with a horizontal orientation, possibly due to fluorosiloxane-induced Zn^{2+} growth along the (002) plane, facilitating the long-term battery cycling [25,50,51]. To visualize the deposition process of Zn^{2+} on the anode, the *in-situ* observation was adopted with a test current density of 20 mA/cm^2. As shown in Fig. 3g, the cross-section of bare Zn becomes quite rugged within 30 min due to the generation of Zn dendrites, and bubbles gradually accumulate at the interface. Notably, the deposition layer on SiFO-Zn remains flat and dense throughout the monitoring period, consistent with the AFM and SEM images. The high zincophilicity of the fluorosiloxane interphase layer significantly reduces the nucleation overpotential of the electrode (Fig. S8 in Supporting information) [52,53]. In conclusion, unlike bare Zn, SiFO-Zn can regulate Zn^{2+} flux, induce horizontal Zn^{2+} deposition and reduce nucleation overpotential (Fig. 2b), offering the potential for excellent battery performance at high current density.

We then tested the long-term cycling performance of SiFO-Zn at a high current density of 20 mA/cm^2. Excitingly, the SiFO-Zn||SiFO-Zn symmetric cell undergoes 22,300 cycles (2600 h) without fluctuations in polarization, with a cumulative capacity of 22.3 Ah/cm^2 (Fig. S9a in Supporting information). Balancing high capacity while achieving stable cycling at high current density is critical for the commercial application of AZMBs [54–56]. Thus, we further increased the discharge capacity to 10 mAh/cm^2 and the current density to 40 mA/cm^2. As shown in Fig. 4a, the SiFO-Zn||SiFO-Zn symmetric cell exhibits a considerably longer cycle life (660 h) in comparison to the Zn||Zn symmetric cell (11 h), with a depth of discharge (DOD) up to 17.1% and a cumulative capacity up to 12.9 Ah/cm^2, exceeding most reports (Fig. 4b) [11,13,16,29,34,35,48,50,51,55,57–59]. To investigate whether the ultra-thin fluorosiloxane interphase layer can induce Zn^{2+} deposition along the (002) plane at high discharge capacity, X-ray diffraction (XRD) tests were performed on the anode before and after 50 cycles (at 10 mAh/cm^2, 40 mA/cm^2). As shown in Fig. S10 (Supporting information), the diffraction peaks at 36.2°, 39.0°, and 43.2° correlate to the Zn (002), (100), and (101) crystal planes (JCPDS No. 87-0713), respectively. The XRD pattern of bare Zn does not change significantly before and after cycling. However, for SiFO-Zn, the intensity ratio of the (002) to (101) plane increases from 0.24 to 0.34, verifying the prominent role of the fluorosiloxane interphase layer in guiding horizontal deposition of Zn^{2+} and inhibiting the dendrite growth even at high anode discharge capacity [60]. Thus, the SiFO-Zn||SiFO-Zn symmetric cell can cycle stably for over 105 h even at a DOD of 34.2% (20 mAh/cm^2, 40 mA/cm^2, Fig. S9b in Supporting information).

For further assessing the anode cycling reversibility, the rate performance tests were conducted at a discharge capacity of 5 mAh/cm^2 and current densities of 10–50 mA/cm^2. As shown in Fig. S11 (Supporting information), the SiFO-Zn||SiFO-Zn symmetric cell operates stably at various current densities (10, 20, 40, and 50 mA/cm^2) with distinctly lower voltage hysteresis (62.6, 76.5, 125.2, and 145 mV) than the Zn||Zn symmetric cell (89.5, 102.9, 162.4, and 197.4 mV). Especially, when the current density is decreased from 50 mA/cm^2 to 10 mA/cm^2, SiFO-Zn||SiFO-Zn is still capable of running over 175 cycles, while Zn||Zn shorts at the 115th cycle. In addition, we assembled the Zn||Cu asymmetric cell to test

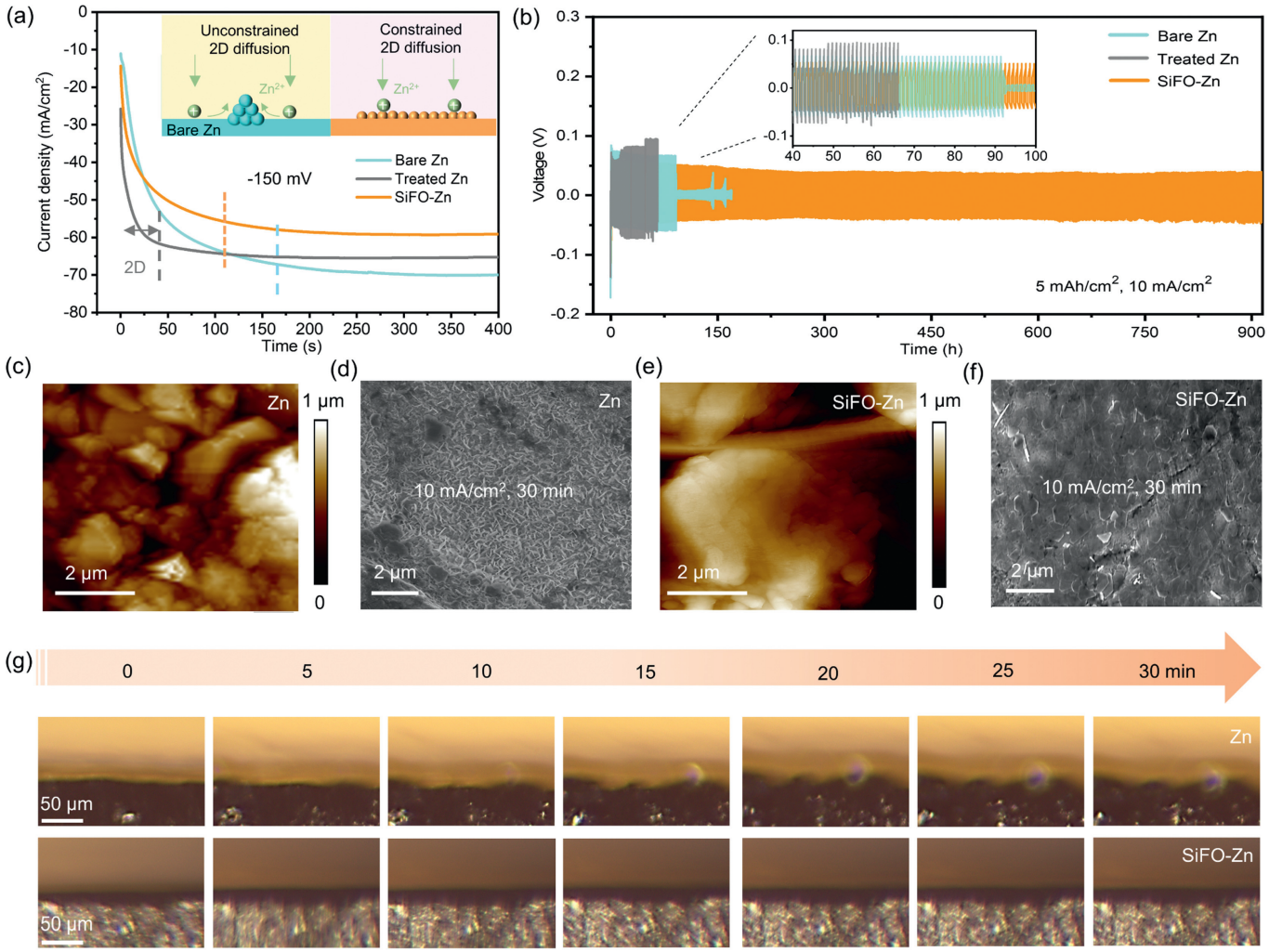

Fig. 3. (a) *I-t* curves for symmetric cells assembled with bare Zn, treated Zn and SiFO-Zn at a constant overpotential of −150 mV. (b) Cycling performance of symmetric cells at 5 mAh/cm^2 and 10 mA/cm^2. Surface AFM 3D height images and SEM images of (c, d) bare Zn and (e, f) SiFO-Zn deposited at 10 mA/cm^2 for 30 min. (g) Optical microscope images of the Zn^{2+} deposition process tested at a current density of 20 mA/cm^2.

the Coulombic efficiency (CE), which is an important parameter for evaluating the Zn^{2+} deposition/dissolution reversibility [20,61]. As shown in Fig. S12 (Supporting information), Zn||SiFO–Cu operates stably for 3800 cycles at 1 mAh/cm^2 and 40 mA/cm^2 with an average high CE of 99.87%. By contrast, Zn||Cu shows severe fluctuations in CE at the 253th cycle and finally fails at the 1252th cycle. Moreover, the voltage-capacity curves of Zn||SiFO–Cu overlap well, with a voltage polarization of only 348.2 mV; while the voltage-capacity curves of Zn||Cu fluctuate drastically, with a voltage polarization as high as 689.9 mV. The above results indicate that owing to the introduction of the fluorosiloxane interphase layer, SiFO-Zn can exhibit excellent cycling performance at high current density.

Due to the excellent cycling performance of SiFO-Zn at high current density, we assembled full cells to explore its potential in fast-charging and flexible devices. Over-thick Zn foils (≥50 μm) have been commonly used as anodes, which cause significant depletion of the full-cell energy density [55]. Here, we chose an ultra-thin Zn foil of 10 μm to match the prepared low-crystallinity MnO_2-birnessite cathode (Fig. S13 in Supporting information) [62], demonstrating a remarkable progress. The CV curves of assembled SiFO-Zn||MnO_2 and Zn||MnO_2 full cells were tested at a scanning rate of 0.5 mV/s (Fig. S14 in Supporting information). In comparison to Zn||MnO_2, SiFO-Zn||MnO_2 exhibits a smaller redox peak gap (348 mV *vs.* 372 mV) and greater response currents, indicating diminished voltage polarization and enhanced charge transfer kinetics [48]. This is further evidenced by the lower R_{ct} of SiFO-Zn||MnO_2 (55 Ω *vs.* 68 Ω for Zn||MnO_2). On this premise, SiFO-Zn||MnO_2 demonstrates an exceptional rate performance (Fig. 4c). As the current density increases from 0.2 A/g to 5 A/g, the capacity gap between SiFO-Zn||MnO_2 (244, 203, 162, 134, 108 mAh/g) and Zn||MnO_2 (241, 190, 152, 121, 86 mAh/g) gradually widens (Fig. S15 in Supporting information). Notably, the capacity of Zn||MnO_2 fluctuates at a high current density of 5 A/g, implying serious dendrite growth and side reactions on the Zn surface. Although the capacity remains nearly unchanged when recovering to 0.2 A/g, the cycling performance of Zn||MnO_2 at 2 A/g verifies that "quantitative change causes qualitative change": The resulting Zn loss and electrolyte pH change lead to rapid capacity attenuation of the battery [63]. For SiFO-Zn||MnO_2, a specific capacity approaching 300 mAh/g is achieved at 0.2 A/g due to the activation of the cathode. Upon increasing the current density to 2 A/g, the capacity of SiFO-Zn||MnO_2 can still be maintained at 205 mAh/g even after another 180 cycles (250 cycles in total) due to the effective inhibition of dendrites and side reactions.

The fast-charging performance of SiFO-Zn||MnO_2 was then evaluated at 2 A/g and 5 A/g, with the corresponding anode current densities of 7 mA/cm^2 and 17.5 mA/cm^2, respectively. As shown in Fig. S16 (Supporting information), SiFO-Zn||MnO_2 achieves 1000

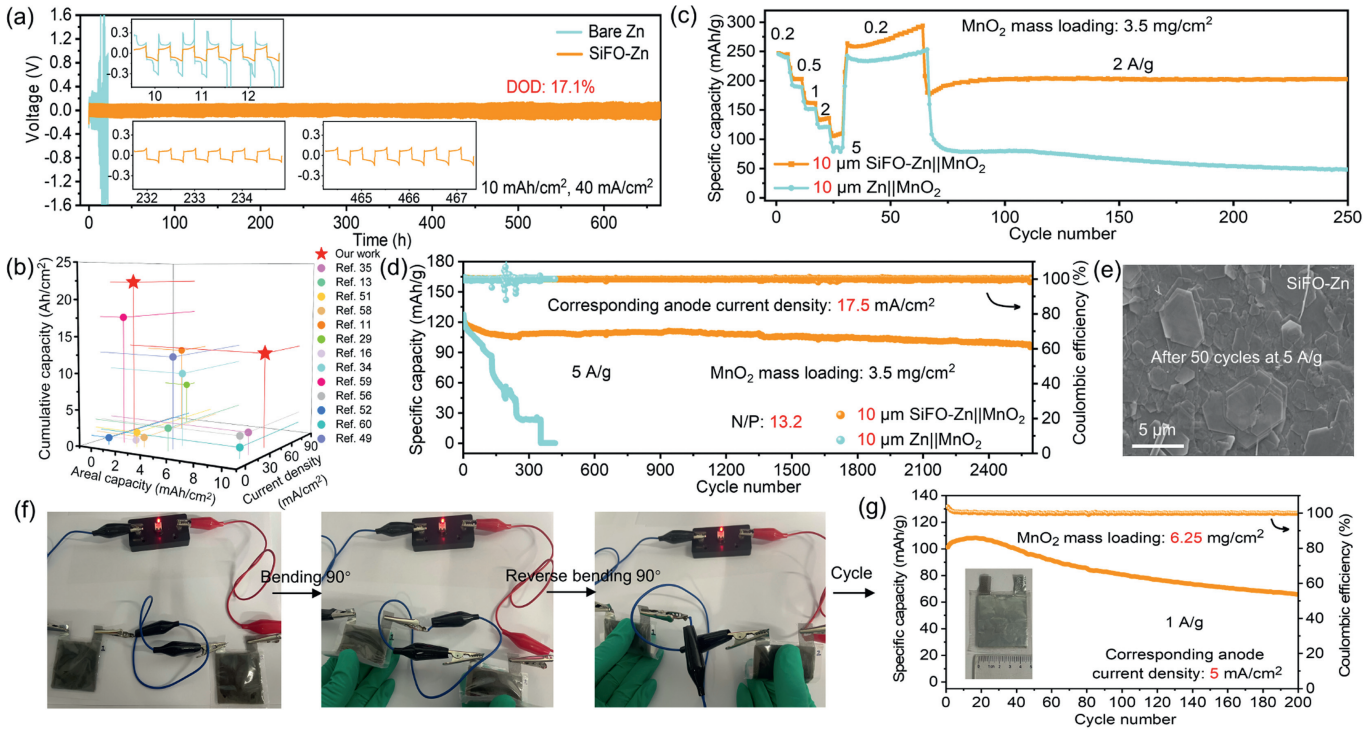

Fig. 4. Cycling performance of symmetric cells at 10 mAh/cm^2 and 40 mA/cm^2. (b) Comparison of the symmetric cycling performance (including current density, discharge capacity and cumulative capacity) in this work with those in previous reports. (c) Rate performance of full cells. (d) Long-term cycling performance of full cells at 5 A/g. (e) SEM image of the SiFO-Zn anode after 50 cycles at 5 A/g. (f) Flexibility demonstration of SiFO-Zn||MnO_2 pouch cell. (g) Cycling performance of SiFO-Zn||MnO_2 pouch cell at 1 A/g after the bending test.

cycles at 2 A/g with almost no capacity attenuation; while the capacity of Zn||MnO_2 is rapidly depleted after only 60 cycles, with severe fluctuations in CE. Based on the highest capacity of the cathode during cycling rather than the theoretical capacity, the negative/positive (N/P) capacity ratios of SiFO-Zn||MnO_2 and Zn||MnO_2 are calculated to be 10.7 and 12.2, respectively. When the current density increases to 5 A/g (N/P ratio: 13.2, Fig. 4d), SiFO-Zn||MnO_2 operates steadily over 2600 cycles, whereas a drastic capacity attenuation is observed within 300 cycles for Zn||MnO_2. In addition, SiFO-Zn||MnO_2 shows lower voltage hysteresis (Fig. S17 in Supporting information), differing from Zn||MnO_2 by 87 mV in the first cycle (Fig. S18 in Supporting information). It is worth noting that, the reduced discharge depth of the anode caused by decreased cathode capacity at 5 A/g extends the cycle life of the full cell [64]. Nevertheless, the performance of SiFO-Zn||MnO_2 is significantly improved compared with Zn||MnO_2 at both 2 A/g and 5 A/g, demonstrating an impressive modification effect of SiFO-Zn. A comparison of full cell performance in this work with those in the recently reported articles is shown in Table S2 (Supporting information) [20,48,51,65–68]. The modification effect is further verified by SEM images of the anode after 50 cycles. As shown in Fig. 4e and Fig. S19 (Supporting information), SiFO-Zn features a flat surface morphology covered with small-sized highly (002)-oriented Zn flakes after cycling, while distinct dendrite clusters are observed on the bare Zn surface. To avoid misjudgment by chance, the SEM images of different regions are provided.

AZMBs possess great potential for flexible wearable electronic devices due to the high flexibility of Zn metal. However, Zn foil has a shape memory effect, which forms wrinkled protrusions after bending, inducing the generation of Zn dendrites, thereby significantly shortening the service life of the devices as well as posing safety hazards [7]. In this study, the fluorosiloxane modification can significantly inhibit Zn dendrites on the surface of Zn foil. Therefore, we used the SiFO-Zn anode to match with a high mass-loading (6.25 mg/cm^2) MnO_2 cathode for assembling a large-size (22.5 cm^{-2}) flexible pouch cell, and further evaluated its performance at high current density. As shown in Fig. 4f, the pouch cell can still light up the LED after reverse bending, showing excellent flexibility. After the bending test, the flexible pouch cell achieves 200 cycles at 1 A/g with an anode current density of 5 mA/cm^2 (Fig. 4g). The phenomenon of initial cycling CE exceeding 100% in the full cell is attributed to the dissolution of Mn in the cathode [63]. In conclusion, SiFO-Zn anode has a broad application prospect in flexible AZMBs, and its excellent cycling performance at high current density provides a possibility for the research and development of fast-charging electronic devices.

In summary, we demonstrate an ultra-thin fluorosiloxane interphase layer of only 20 nm for fast-charging flexible AZMBs. In such an interphase layer, the formation of Si-O-Zn bonds between fluorosiloxane and hydroxyl–rich Zn contributes to interfacial stability, and the Si-O-Si bonds generated by fluorosiloxane molecule condensation facilitate an even electric field distribution. Furthermore, the introduced highly electronegative F atoms effectively regulate the Zn^{2+} flux, induce the horizontal Zn^{2+} deposition, and enhance the charge transfer kinetics. Thus, the modified Zn anode (SiFO-Zn) can effectively inhibit dendrites and side reactions, thereby improving the electrochemical performance of the battery. Excitingly, the SiFO-Zn||SiFO-Zn symmetric cell can cycle stably even at an ultra-high current density of 40 mA/cm^2, with a cumulative capacity up to 12.9 Ah/cm^2. When the 10 μm-thick SiFO-Zn anode is matched with MnO_2 cathode, the full cell achieves 2600 cycles with almost no capacity attenuation at a high current density of 5 A/g. Further matched with a high mass-loading (6.25 mg/cm^2) MnO_2 cathode, the flexible pouch cell withstands reverse bending without short-circuit, and exhibits excellent cycling performance at 1 A/g. This facile, low-energy consumption, and scalable interfacial modification strategy can effectively improve the performance of

Zn anodes at high current density, laying the foundation for the development of dendrite-free, fast-charging, and flexible AZMBs.

Declaration of competing interest

The authors declare that they have no known competing financial interests or personal relationships that could have appeared to influence the work reported in this paper.

CRediT authorship contribution statement

Yuhuan Meng: Writing – original draft, Visualization, Validation, Formal analysis, Data curation, Conceptualization. **Long Zhang:** Writing – review & editing, Supervision, Resources, Project administration, Funding acquisition. **Lequan Wang:** Investigation. **Junming Kang:** Investigation. **Hongbin Lu:** Writing – review & editing, Supervision, Resources, Project administration, Funding acquisition.

Acknowledgments

This work was supported by the National Natural Science Foundation of China (Nos. 22075048, 52201201), Shaanxi Yanchang Petroleum Co., Ltd. (No. 18529), Yiwu Research Institute of Fudan University (No. 20-1-06), the Shanghai International Collaboration Research Project (No. 19520713900), the State Key Laboratory of Molecular Engineering of Polymers (Fudan University, No. K2024-36), and the State Key Lab of Advanced Metals and Materials (No. 2022Z-11).

Supplementary materials

Supplementary material associated with this article can be found, in the online version, at doi:10.1016/j.cclet.2024.110025.

References

[1] S. Yang, H. Du, Y. Li, et al., Green Energy Environ. 8 (2023) 1531–1552.
[2] Z. Jiang, K. Yin, R. Pan, et al., Small 19 (2023) 2302995.
[3] H. Yu, H. Yao, Y. Zheng, et al., Adv. Funct. Mater. 34 (2024) 2311038.
[4] W. Wu, Y. Deng, G. Chen, Chin. Chem. Lett. 34 (2023) 108424.
[5] C. Zhu, P. Li, G. Xu, H. Cheng, G. Gao, Coord. Chem. Rev. 485 (2023) 215142.
[6] Q. Liu, Z. Yu, Q. Zhuang, et al., Adv. Mater. 35 (2023) 2300498.
[7] W. Wang, C. Li, S. Liu, et al., Adv. Energy Mater. 13 (2023) 2300250.
[8] Q. Yang, G. Liang, Y. Guo, et al., Adv. Mater. 31 (2019) 1903778.
[9] Y. Geng, L. Miao, Z. Yan, et al., J. Mater. Chem. A 10 (2022) 10132–10138.
[10] X. Yan, X. Huang, Y. Liu, et al., Chin. Chem. Lett. 35 (2024) 109426.
[11] D. Wang, H. Liu, D. Lv, et al., Adv. Mater. 35 (2023) 2207908.
[12] S.D. Pu, C. Gong, Y.T. Tang, et al., Adv. Mater. 34 (2022) 2202552.
[13] P. Xiao, Y. Wu, J. Fu, et al., ACS Energy Lett. 8 (2023) 31–39.
[14] Y. Yang, H. Yang, R. Zhu, H. Zhou, Energy Environ. Sci. 16 (2023) 2723–2731.
[15] P. Sun, L. Ma, W. Zhou, et al., Angew. Chem. Int. Ed. 60 (2021) 18247–18255.
[16] H. Wu, W. Yan, Y. Xing, et al., Adv. Funct. Mater. 34 (2024) 2213882.
[17] X. Chen, M. Li, Q. Li, et al., Energy Environ. Mater. 6 (2023) e12480.
[18] H. Liu, J. Li, X. Zhang, et al., Adv. Funct. Mater. 31 (2021) 2106550.
[19] X. Zhou, R. Chen, E. Cui, et al., Energy Storage Mater 55 (2023) 538–545.
[20] Q. Liu, Y. Wang, X. Hong, et al., Adv. Energy Mater. 12 (2022) 2200318.
[21] B. Li, X. Zhang, T. Wang, et al., Nano-Micro Lett. 14 (2022) 6.
[22] J. Yang, B. Yin, Y. Sun, et al., Nano-Micro Lett. 14 (2022) 42.
[23] J. Cui, P. Yin, A. Xu, et al., Nano Energy 93 (2022) 106837.
[24] W. Lu, B.B. Xie, C. Yang, et al., Small 19 (2023) 2302629.
[25] Z. Zhao, R. Wang, C. Peng, et al., Nat. Commun. 12 (2021) 6606.
[26] L. Wang, L. Zhang, Y. Meng, et al., Sci. China Mater. 66 (2023) 4595–4604.
[27] Z. Shi, M. Yang, Y. Ren, et al., ACS Nano 17 (2023) 21893–21904.
[28] J. Li, B. He, Y. Zhang, et al., Small 18 (2022) 2200567.
[29] W. Yuan, X. Nie, G. Ma, et al., Angew. Chem. Int. Ed. 62 (2023) e202218386.
[30] J. Zhang, W. Huang, L. Li, et al., Adv. Mater. 35 (2023) 2300073.
[31] R. Yi, Y. Mao, Y. Shen, L. Chen, J. Am. Chem. Soc. 143 (2021) 12897–12912.
[32] L. Wang, U.S. Schubert, S. Hoeppener, Chem. Soc. Rev. 5 (2021) 654–657.
[33] H. Fan, D. Shi, M. Ding, et al., Prog. Org. Coat. 138 (2020) 105392.
[34] S.H. Park, S.Y. Byeon, J. Park, C. Kim, ACS Energy Lett. 6 (2021) 3078–3085.
[35] J. Dong, H. Peng, J. Wang, et al., Energy Storage Mater 54 (2023) 875–884.
[36] Y. Zhu, Z. Huang, M. Zheng, et al., Adv. Funct. Mater. 34 (2024) 2306085.
[37] H. Gan, J. Wu, F. Zhang, R. Li, H. Liu, Energy Storage Mater. 55 (2023) 264–271.
[38] K. Wang, T. Su, C. Shao, W. Ren, R. Sun, ACS Sustain. Chem. Eng. 10 (2022) 16225–16237.
[39] Y. Li, N.E. Vecchio, W. Lu, Spectrochim. Acta A 105 (2013) 213–217.
[40] Y. Sato, R. Hayami, T. Gunji, J. Solgel Sci. Technol. 104 (2022) 36–52.
[41] S.L. Warring, D.A. Beattie, A.J. Mcquillan, Langmuir 32 (2016) 1568–1576.
[42] L. Cao, D. Li, T. Pollard, et al., Nat. Nanotechnol. 16 (2021) 902–910.
[43] H. Chen, J. Chen, W. Zhang, et al., J. Mater. Chem. A 8 (2020) 2254–2264.
[44] T. Tan, P. Lee, M. Marium, N. Zettsu, D.Y.W. Yu, ACS Appl. Energy Mater. 5 (2022) 11254–11262.
[45] C. Chang, S. Hu, T. Li, et al., Energy Environ. Sci. 17 (2024) 680–694.
[46] S. Jiao, J. Fu, M. Wu, T. Hua, H. Hu, ACS Nano 16 (2022) 1013–1024.
[47] W. Dong, C. Liu, X. Ji, et al., Small Method. 8 (2024) 2300799.
[48] H. Liu, Q. Ye, D. Lei, et al., Energy Environ. Sci. 16 (2023) 1610–1619.
[49] B. Ren, S. Hu, A. Chen, et al., Adv. Energy Mater. 14 (2024) 202302970.
[50] H. Wang, Y. Chen, H. Yu, et al., Adv. Funct. Mater. 32 (2022) 2205600.
[51] H. Yu, Y. Chen, H. Wang, et al., Nano Energy 99 (2022) 107426.
[52] H.J. Kim, S. Kim, K. Heo, et al., Adv. Energy Mater. 13 (2023) 2203189.
[53] J. Chen, W. Zhao, J. Jiang, et al., Energy Storage Mater. 59 (2023) 102767.
[54] Z. Hou, Y. Gao, H. Tan, B. Zhang, Nat. Commun. 12 (2021) 3083.
[55] L. Ma, Q. Li, Y. Ying, et al., Adv. Mater. 33 (2021) 2007406.
[56] X. Xu, S. Li, Z. Cao, S. Yang, B. Li, Adv. Energy Mater. 14 (2024) 202303971.
[57] S. Liu, H. Lin, Q. Song, J. Zhu, C. Zhu, Energy Environ. Mater. 6 (2023) e12405.
[58] D. Lv, H. Peng, C. Wang, et al., J. Energy Chem. 84 (2023) 81–88.
[59] Z. Guo, L. Fan, C. Zhao, et al., Adv. Mater. 34 (2022) 2105133.
[60] X. Cai, X. Wang, Z. Bie, et al., Adv. Mater. 36 (2024) 2306734.
[61] H. Yan, S. Li, Y. Nan, S. Yang, B. Li, Adv. Energy Mater. 11 (2021) 2100186.
[62] N. Qiu, H. Chen, Z. Yang, S. Sun, Y. Wang, Electrochim. Acta 272 (2018) 154–160.
[63] H. Yang, T. Zhang, D. Chen, et al., Adv. Mater. 35 (2023) 2300053.
[64] J. Li, Q. Lin, Z. Zheng, et al., ACS Appl. Mater. Interfaces 14 (2022) 12323–12330.
[65] Y. Zou, Y. Su, C. Qiao, et al., Adv. Energy Mater. 13 (2023) 2300932.
[66] X. Yang, J. Lv, C. Cheng, et al., Adv. Sci. 10 (2023) 2206077.
[67] Q. Cao, H. Gao, Y. Gao, et al., Adv. Funct. Mater. 31 (2021) 2103922.
[68] Y. Zeng, P.X. Sun, Z. Pei, et al., Adv. Mater. 34 (2022) 2200342.